

A global aerosol model forecast for the ACE-Asia field experiment

Mian Chin,^{1,2} Paul Ginoux,³ Robert Lucchesi,^{4,5} Barry Huebert,⁶ Rodney Weber,¹
Tad Anderson,⁷ Sarah Masonis,⁷ Byron Blomquist,⁶ Alan Bandy,⁸ Donald Thornton⁸

Abstract. We present the results of aerosol forecast during the ACE-Asia field experiment in spring 2001, using the Georgia Tech/Goddard Global Ozone Chemistry Aerosol Radiation and Transport (GOCART) model and the meteorological forecast fields from the Goddard Earth Observing System Data Assimilation System (GEOS DAS). The model provides direct information on aerosol optical thickness and concentrations for effective flight planning, while feedbacks from measurements constantly evaluate the model for successful model improvements. We verify the model forecast skill by comparing model predicted aerosol quantities and meteorological variables with those measured by the C-130 aircraft. The GEOS DAS meteorological forecast system shows excellent skills in predicting winds, relative humidity, and temperature, with skill scores usually in the range of 0.7 – 0.99. The model is also skillful in forecasting pollution aerosols, with most scores above 0.5. The model correctly predicted the dust outbreak events and their trans-Pacific transport, but it constantly missed the high dust concentrations observed in the boundary layer. We attribute this “missing” dust source to desertification regions in the Inner Mongolia Province in China, which have developed in recent years but were not included in the model during forecasting. After incorporating the desertification sources, the model is able to reproduce the observed boundary layer high dust concentrations over the Yellow Sea. We demonstrate that our global model can not only account for the large-scale intercontinental transport, but also produce the small-scale spatial and temporal variations that are adequate for aircraft measurements planning.

1. Introduction

The Asian Pacific Regional Aerosol Characterization Experiment (ACE-Asia), which took place during the spring of 2001 over the Asian-Pacific region, was designed to investigate aerosol properties and their radiative forcing in the anthropogenically modified atmosphere of eastern Asia and northwestern Pacific. The intensive field study (March 31 – May 4, 2001) of ACE-Asia was concentrated over the Yellow Sea and the Sea of Japan, involving measurements from several aircraft and ships that were coordinated with the surface network and satellite observations to sample the Asian outflow [Huebert et al., 2003].

East Asia is an important source region of all major tropospheric aerosol types. It has been estimated that fast economic development, large areas of desert, and intensive forest and agriculture fires in the region contribute to one-fourth to one-third of total global emissions of SO₂, organic matter, soot, and dust [e.g. Chin et al. 2000, 2002; Ginoux et al. 2001; and references therein]. During the spring, the transport of airmasses from the Asian continent to the western Pacific is at its maximum and, as a result, sources of anthropogenic and natural aerosols over Asia have a maximum impact on the Pacific and downwind regions. Depending on meteorological conditions, such as wind direction, convection intensity, cloud coverage, and precipitation, the composition of aerosols over the ACE-Asia experimental area is either a multi-component aerosol mixture, or dominated by one specific type of aerosol. Long-range transport from Europe, Africa, and western Asia would further add to the complexity of aerosol distributions and compositions over the western

Pacific. A successful field experiment depends on careful daily planning, which requires the mission scientists to make optimal decisions based on the best available information.

This paper summarizes the results of our aerosol forecast during the ACE-Asia field experiment using the Georgia Tech/Goddard Global Ozone Chemistry Aerosol Radiation and Transport (GOCART) model. During the intensive field study period indicated above, we used the GOCART model to provide a 24- to 96-hour forecast of aerosols everyday for mission scientists and measurement teams to make daily flight plans. Included in the products are horizontal and vertical distributions of aerosol composition, extinction, and optical thickness due to sulfate, dust, black carbon (BC), organic carbon (OC), and sea-salt aerosols. The participation of a model in field experiments has two clear advantages. First, the aerosol forecast from the model provides direct information to mission scientists and measurement teams as to what should be expected on the amount, type, and distribution of aerosols as well as the duration of large episodes such as dust storms. This information is not readily available from the meteorological forecasts traditionally used in previous field programs. Second, the measurements equipped with such direct information provide feedback as an instantaneous evaluation on the modeled processes, such as sources and transport, enabling us to constantly improve the model. Close interaction between the model and measurements established during the ACE-Asia has made the post-mission data analysis fruitful.

While our extensive post-mission modeling and analysis of the ACE-Asia data will be forthcoming in several manuscripts currently in preparation, we focus in this paper on verifying the

GOCART model forecast performance and assessing the value of the model's involvement in the ACE-Asia field experiment. We begin by describing the GOCART aerosol forecast processes during the ACE-Asia 2001 fieldwork (section 2). We then show the model forecast products and evaluate the model skill by comparing the forecast products with the aircraft observations, demonstrating how the measurements help improve the model (section 3). After discussing the strengths and limitations of the model (section 4), we will present our conclusions (section 5).

2. Aerosol Forecast Process

2.1. The GOCART Model

Aerosol simulations in the GOCART model include major tropospheric aerosol types of sulfate, dust, OC, BC, and sea-salt. The model uses assimilated meteorological fields from the Goddard Earth Observing System Data Assimilation System (GEOS DAS), containing winds, temperature, pressure, specific and relative humidity, cloud mass flux, cloud fraction, precipitation, boundary layer depth, surface winds, and surface wetness. Physical processes in the model are emission, advection, convection, boundary layer mixing, wet deposition (rainout and washout), dry deposition, and settling. Chemical processes include gas and aqueous phase reactions that convert sulfate precursors (dimethylsulfide and SO_2) to sulfate. A dust source parameterization has been constructed in the GOCART model, where locations of the dust sources are determined at the topographic depression areas with bare soil surfaces, while the dust uplifting probability is defined according to the degree of depression. The model simulation of dust aerosol has been found to be consistent with surface, lidar, and satellite observations [Ginoux et al. 2001]. The biomass burning emissions of BC and OC are based on the burned biomass inventory which is estimated using the satellite observations of fire counts and aerosol index [Duncan et al. 2003]. The new biomass burning emissions have since significantly improved the modeled seasonal variations of biomass burning and have made interannual biomass burning simulation possible [Chin et al. 2002]. Detailed description of the model has been presented elsewhere [Chin et al. 2000a, b; Ginoux et al. 2001; Chin et al. 2002].

Emissions in our forecast mode were basically the same as described in Chin et al. 2002. Anthropogenic emissions of SO_2 were taken from the Emission Database for Global Atmospheric Research [Olivier et al. 1996], and those of BC and OC were from a global dataset [Cooke et al., 1999]. We used the climatological biomass burning emissions of BC, OC, and SO_2 for March, April, and May, and only considered the continuously erupting volcanic emissions. Sea salt emissions with 4 size bins ($0.1 - 10 \mu\text{m}$) were calculated as a function of surface wind speed [Gong et al., 1997; Monahan et al., 1986]. Following Ginoux et al. [2001], emission rates of 7 dust size groups ($0.1 - 6 \mu\text{m}$) were calculated as

$$E_p = S_d f_p u^2 (u - u_t) \quad (1)$$

where E_p is the emission rate for size group p , S_d is the probability source function, which is the probability of sediments accumulated at the topographic depression regions

with bare surface, f_p is the fraction of size group p within the soil, u is the surface wind speed, and u_t is the threshold velocity of wind erosion determined by particle size and surface wetness. Note that while the anthropogenic emission rates were kept constant in the model, dust and sea-salt emissions had very strong temporal variations, depending on surface and meteorological conditions especially wind speed. Figure 1 shows the emissions for April 2001 for sulfur (SO_2 and DMS), carbonaceous aerosols (BC + OC), dust, and sea salt in our forecast mode. Updated emissions from sporadically erupting volcanoes, biomass burning, and anthropogenic sources are incorporated in the analysis mode as the information has become available after the field operation. Dust source function S_d in the analysis mode is also modified based on the information from the ACE-Asia measurements (see section 3). These updated emissions (not shown) are currently being used in our post-mission analysis mode.

The aerosol optical thickness was determined from the mass concentrations, size distributions, refractive indices, and hygroscopic properties of individual type of aerosols. We assumed lognormal size distributions for sulfate, OC, and BC aerosols with effective dry radii of 0.16 , 0.09 , and $0.04 \mu\text{m}$, respectively, and lognormal size distributions for each discrete dust and sea salt size groups. The wavelength-dependent refractive indices are based on the Global Aerosol Data Set (GADS) [Köpke et al. 1997]. With the exception of dust, aerosols are considered to have different degrees of hygroscopic growth rate with ambient moisture. The hygroscopic growth factors are based on the GADS data and others [d'Almeida et al. 1991]. For example, at ambient relative humidity (RH) of 80%, the radius of wet sulfate, OC, BC, and sea-salt aerosols are a factor of 1.6, 1.5, 1.2, and 2 larger than their dry size. We assume that dust particle sizes do not change with RH, since dust aerosols contain little hygroscopic material and their radiative properties are relatively insensitive to changes in RH [Li-Jones et al. 1999]. All aerosol particles are treated as external mixtures due to the difficulties and high uncertainties in describing the degree of internal mixing (details of aerosol optical parameters and the calculation of optical thickness in the GOCART model have been provided in Chin et al. 2002).

2.2. GEOS DAS Meteorological Products

The meteorological data used to run the GOCART model are generated by the GEOS DAS, which is developed and run operationally by the NASA Goddard Data Assimilation Office (DAO). The GEOS DAS version 3 (GEOS-3) products were used in the model during the 2001 ACE-Asia field experiment. The GEOS-3 system is run by the DAO in two assimilation modes: the First Look assimilation and the Late Look assimilation. The First Look runs 4 times/day, about 8-15 hours behind real time, analyzing meteorological input data from conventional and satellite observations available at the time. The input data include upper air winds, geopotential heights, pressure, total precipitable water, sea-surface winds, sea-surface temperature, and sea-surface ice. The Late Look system configuration is similar to that for the First Look but it runs 2 to 3 weeks behind real time, allowing a more complete set of input observations to be integrated into the assimilation

system. The First Look system also produces 5-day (0 – 120-hour) forecast products twice a day initialized at 0 and 12 hours Universal Time (UT). The forecast products are generated from the same general circulation model used in the assimilation, except that there is no observation data input to the system. The forecast system is initialized by the First Look assimilation output and runs 5 days forward. Table 1 lists the GEOS-3 prognostic and diagnostic fields used in our aerosol forecast and simulations.

2.3. Aerosol Forecast

During the ACE-Asia period, we used the GEOS-3 First Look assimilation products to initialize the GOCART model, and the First Look 0 UT forecast products to generate aerosol forecast products. The DAO provided the forecast products at $2^\circ \times 2.5^\circ$ horizontal resolution, while the assimilated products were at $1^\circ \times 1^\circ$. We regridded the $1^\circ \times 1^\circ$ assimilated GEOS-3 data to $2^\circ \times 2.5^\circ$ grid in order to obtain a consistent resolution and reduce the computational time. The vertical resolution in the original GEOS-3 data contains 48 sigma layers, with 22 layers above 30 mb. We aggregated the top 22 layers into 4 to reduce the total number of layers to 30 in our tropospheric simulations. The model layer thickness increases gradually from surface to the model top. Below 3 km, the vertical resolution varies from 24 m to 900 m. Above 3 km, the vertical resolution changes from 1 km to about 1.5 km near the tropopause. The GOCART model products were in the same spatial resolution as the meteorological data (i.e. $2^\circ \times 2.5^\circ$, or about 200 km in mid-latitudes, and 30 vertical layers), and were saved every 3 hours. Table 2 lists our 24 – 96-hour forecast products provided for the field operations.

Our daily forecast procedure involved processing the GEOS-3 data, running the GOCART forecast model, generating figures and animation, providing results on the website as well as to the Joint Office of Science Support (JOSS) field catalog for easy access in the operation field, and, finally, briefing the science team in the Operations Center for flight planning. The daily operational procedure is illustrated in Figure 2.

3. Results

3.1. Distributions of Anthropogenic and Dust Aerosols

A major advantage of 3-D chemistry transport model forecasting for a field operation is its capability of making available the direct information of distributions, levels, and the evolution of aerosol species that are being measured in the experiment. This capability is especially important for ACE-Asia since the distribution of aerosols shows a high spatial and temporal heterogeneity. Figure 3 illustrates the 24-hour model forecast products of sulfate and dust optical thickness for April 2 and April 12, 2001, which show very different spatial distributions of aerosols over the eastern Asia/western Pacific region. On April 2, 2001 (top row, Figure 3), the model indicated that both Yellow Sea and the Sea of Japan were to receive large amounts of pollution from China with a total sulfate AOT of 0.3 – 0.5. In comparison, there were also dust aerosols over the same region but with much lower AOT

values. The model forecast for April 12 shows completely different distributions (bottom row, Figure 3). In fact, there was a major dust outbreak on April 6-9, 2001, mainly from the Gobi and Mongolia plateau, east of the Taklimaken desert. The passage of a cold front through China on April 9 – 11 swept the polluted air from eastern China to the sea, leaving eastern China relatively “pollution free” (sulfate AOT from 0.05 to 0.15) while causing a pollution band located along 135°E , more than a thousand km away from the coast. However, the same front brought a large dust plume with it, filling the eastern China and coastal regions with relatively heavy dust. This type of information, which is difficult to extract from the traditional weather forecast, made flight planning more effective.

The dust plume generated from the aforementioned dust storm traveled all the way across the North Pacific and eventually reached North America within a few days. The evolution and trans-Pacific transport of dust are demonstrated in Figure 4. The model 24-hour forecast of dust aerosol optical thickness for April 8, 11, and 14 are plotted in the left column with the GEOS-3 forecast wind vectors at 4 km superimposed to indicate the general transport direction. On April 8, 2001, dust emitted from the source region and was transported downwind to the Pacific. At the same time, there was another branch of dust wrapping around a low-pressure system centered at 50°N , 125°E (top panel, left column in Figure 4). The prevailing NW winds over central China and SW winds near the east coast switched the dust plume from west-east direction on April 8 to southwest-northeast direction on April 11, with dust plume penetrating to as far south as 20°N over eastern China (middle panel). The dust plume meandered in a wavy pattern across the Pacific Ocean. On April 14, the entire west coast of North America from 30°N to 60°N were heavily influenced by the dust from Asia (bottom panel), which was moving further toward the U.S. inland. To verify the model forecast of dust transport on a large spatial scale, we plot on the right column in Figure 4 the aerosol index (AI) from the satellite sensor of Total Ozone Mapping Spectrometer (TOMS) for the same days (the TOMS over-pass is at about 11:10 am local time). Although the TOMS AI is usually more sensitive to the UV-absorbing aerosols at altitudes above 2 km than those below, and could be distorted by the presence of clouds, it is an excellent indicator of the presence of UV-absorbing aerosols, such as dust and black carbon [Hsu et al., 1996; Herman et al., 1997; Torres et al., 1998]. The TOMS AI in Figure 4 shows very similar patterns of aerosol plume evolution and the trans-Pacific transport as predicted by the model, proving that the GEOS-3 forecast winds are quite realistic. It should be pointed out that our dust source has been improved considerably after the ACE-Asia forecast operation such that the corrected dust AOT is typically a factor of 2 higher than that shown here. We will discuss the dust source later in the text (section 3.3).

3.2. Verification of Model Forecasts

Although the model can effectively simulate the regional and global aerosol distributions and account for the long-range transport, one particular question is how well the relatively coarse resolution model can predict the variations and

characteristics of aerosols at the spatial and temporal scale of the aircraft measurements for mission support. We address this question here by verifying the model forecast results with aircraft observations and comparing the model predicted and measured vertical profiles.

3.2.1. Data and model results. During the intensive operation period of March 31 – May 4 2001, two aircraft from the U.S., a C-130 and a Twin Otter, were making measurements in the area of the Yellow Sea and the Sea of Japan. Here we verify our model performance with observations taken from the C-130 aircraft because of its more extensive spatial and temporal coverage than the Twin Otter. A total of 19 research flights (RF) were conducted with the C-130; the dates and the flight track are shown in Figure 5. We choose 4 quantities to verify the model, as they are representative of the most important aerosol characteristics: concentrations of dust, sulfate (a major component of pollution aerosol), and SO_2 (sulfate precursor), and total aerosol extinction at 550 nm. Since there was no direct measurement of dust mass, we use the soluble Ca^{2+} data as a surrogate of dust, assuming a 6% mass content of soluble Ca^{2+} in dust. This assumption is based on the dust measurements in China [Zhang et al. 2003], which indicate a 6 – 12% Ca^{2+} content in dust mass, with about half being soluble. Table 3 lists the datasets used in this study. The sulfate and Ca^{2+} data used here are from two different instruments: the Particle-Into-Liquid Sampler (PILS, Weber et al. 2001) and the Total Aerosol Sampler (TAS, Jena Kline, personal communication, 2003). The PILS dataset has much finer spatial and temporal resolutions than the TAS due to its faster instrument response time (3-4 min), but it is limited to measuring aerosol size less than 1.3 μm . The TAS, on the other hand, measures both sub-micron and super-micron particles, but it requires longer integration time (20 – 60 min), thus having only a few data points for each flight. Therefore, we use the PILS data to evaluate the model predicted aerosol distribution patterns and the TAS data to compare the aerosol concentrations. In addition to aerosol and precursor species, meteorological variables of wind speed, wind direction, RH, and temperature, which were directly measured on the C-130, are also used to compare with the GEOS-3 meteorological forecast products.

As seen in Table 3, the data acquisition frequency varies by orders of magnitudes among different instruments. Here we use the 10-min merged dataset to attribute the data in a common frame of time and space. At a typical speed of 100 – 120 m s^{-1} , the C-130 aircraft travels about 60 – 70 km distance in 10 min at a cruise altitude. This horizontal scale is about 3 – 4 times finer than the model resolution. Vertically, however, the aircraft can move more than 1 km in 10 min, crossing several model layers at low altitudes but comparable to the model vertical resolution at higher altitudes. We choose the 10-min merged data as the best compromise between the different sampling frequency datasets and between the different scales of model and data. For each 10-min merged data point, the corresponding location of the model point was determined as the center of the gridbox that contains the latitude, longitude, and altitude of the data point at the closest time to the data sampling time.

3.2.2. Skill scores of model forecasts. Two most commonly used statistics to quantify the correspondence

between two fields (e.g. forecast and observation) are correlation coefficient (R) and the root-mean-square error (E). While the R tells similarity of the pattern, the E counts difference in the two fields. A skillful model should be able to predict both the pattern and the magnitudes of variations. We use the following definition of skill score [Taylor, 2001] to mark the overall model performance:

$$S = \frac{4(1+R)}{(\sigma_f + 1/\sigma_f)^2(1+R_0)} \quad (2)$$

Where σ_f is the ratio of the standard deviation of forecast to that of observation, and R_0 is the maximum attainable correlation coefficient. The skill score varies between 0 (no skill) and 1 (perfect skill). As seen in equation (2), when R approaches R_0 and the model variance approaches the observed variance, S moves toward 1. We assume that R_0 equals 1, although in reality the maximum attainable value should always be less than 1 due to the intrinsic differences (e.g. spatial and time resolution) between the model and observation.

The model 24-hour forecast skill scores, S , and correlation coefficients, R , for the 4 meteorological variables (wind speed, wind direction, relative humidity, and temperature) and 4 aerosol-related quantities (dust, sulfate, SO_2 concentrations and total aerosol extinction) for each C-130 research flight are summarized in Figure 6. Here, the S and R are calculated from the 10-min merged data and the corresponding model results described in section 3.2.1 (total number of data points in each flight is indicated at the bottom of each panel). As mentioned earlier, we use the PILS data for the statistics for each flight since there were too few data points from the TAS instrument in each flight to produce meaningful statistics. Because the PILS measures only sub-micron particles while most dust particles are in the super micron size range, we show in Figure 6 only the R values for dust, since the S values would be meaningless in this case. We further assign these scores into 6 letter score groups for easy comprehension: X , when $S \geq 0.9$; A , when $0.9 \geq S > 0.7$; B , when $0.7 \geq S > 0.5$; C , when $0.5 \geq S > 0.3$; D , when $0.3 \geq S > 0.1$; and F , when $S < 0.1$. The letter scores are also indicated in Figure 6.

The GEOS-3 assimilation system shows remarkable meteorological forecast skill, with a majority of the scores in the X and A category. Among the 4 meteorological variables, the forecast temperature has the highest scores (> 0.99) across all 19 flights while the scores for the wind direction are more variable, from 0.3 to 0.9. This is expected, since the temperature is much less changeable than the wind direction on sub- spatial and temporal scale. The scores for the GOCART model forecasted aerosol fields, on the other hand, show large fluctuations from flight to flight, from near zero to 0.9. Several factors contributed to the discrepancies between the forecasts and observations. In the forecast mode, the model did not include the volcanic emission from the Miyakajima volcano which started erupting in September 2000. The volcanic plume was encountered during RF 11 and 12, where the model shows the worst SO_2 scores (between 0.1 and 0.2). Figure 6 points out large differences between the predicted and observed dust concentrations, with half of the R values below 0.3, and $1/4$ of them negative. Although the uncertainties in converting Ca^{2+} to dust certainly contributed to

the discrepancy, as we used a constant value of soluble Ca^{2+} content in dust while this content could vary by a factor of 2, it is the uncounted dust source in the model during the forecast phase that has caused the large differences. We will discuss this “missing” dust source later.

3.2.3. Comparison of vertical profiles. We compare in detail the model forecasts with data from eight selected flights in Figure 7, with four of them measured mainly pollution aerosols (RF 6, 9, 14, 16, Figure 7a), and another four encountered high dust concentrations (RF 5, 6, 10, 13, Figure 7b). The model in general shows high skill in predicting pollution aerosol distributions, as the observed vertical profiles of extinction and concentrations of sulfate and SO_2 match model forecast very well, with the highest values located in the boundary layer. In the absence of large dust storm influences, the model predicts a “background” dust level of $15 - 30 \mu\text{g m}^{-3}$ with a maximum at $4 - 6 \text{ km}$ (Figure 7a). This feature can be seen in the observations (2nd row in Figure 7a), although the quantitative comparison is difficult because, as mentioned previously, the PILS (open circles) measured mainly sub-micron aerosols while the TAS (solid circles) had only limited data for each flight. Even so, it is obvious that the model forecast consistently underestimates the dust amount in the boundary layer. This underprediction is further revealed in Figure 7b where large dust amount was observed, especially during RF 6 (April 11) and RF 13 (April 24). While the model had correctly predicted the dust outbreak event (see Figure 4) that prompted the aircraft to measure the dust plume over the Yellow Sea on April 11, it underpredicted the dust concentration and the total aerosol extinction at the altitudes below 2 km by a factor of 4 to 8 in RF 6. On April 24, the model predicted a background level dust over the Yellow Sea, from $<10 \mu\text{g m}^{-3}$ below 2 km to about $30 \mu\text{g m}^{-3}$ at 6 km , but the RF 13 came across very high dust concentrations below 2 km , with concentrations near $450 \mu\text{g m}^{-3}$ and total aerosol extinction at 0.6 km^{-1} . In addition, the model did not capture the large dust and sulfate peak at 4 km in RF 5 over the Sea of Japan (1st column in Figure 7b).

To examine the overall aerosol vertical characteristics over the ACE-Asia measurement area, we assemble the data and the model forecasts into 2 groups. Group 1 contains data from 8 flights ((RF 4, 6, 7, 10, 13, 14, 15, 18), which covered a very similar L-shaped track, i.e. leaving westward from the Operations Center at Iwakuni, Japan along $33^\circ - 34^\circ\text{N}$ latitude to the Yellow Sea and then northward along $123^\circ - 124^\circ\text{E}$ over the Yellow Sea (see Figure 5, RF 4 for example). Group 2 consists of the remaining 11 flights. Figure 8a and 8b summarizes the overall comparison of aerosol extinctions and concentrations as well as the meteorological parameters for these 2 groups. For clarity, we averaged the 10-min merged data and corresponding model forecast products into the altitude bins according to the model vertical resolution, and the statistics (S , R , E) are calculated using the averaged points. Consistent with their skill scores (Figure 6), the GEOS-3 meteorological forecast products have accurately predicted the vertical variations of winds, relative humidity, and temperature with correlation coefficients being $0.91 - 0.997$, except the wind directions in group 1 where the correlation coefficient is not as high (0.76). The GEOS-3 also overpredicts the relative

humidity at $6 - 7 \text{ km}$ for group 2. While both the model and observations agree that SO_2 , sulfate, and total aerosol extinction decrease with the increase of altitude, the model has predicted a minimum dust concentrations in the boundary layer for both group 1 and 2 when the C-130 has observed very high dust concentrations in the boundary layer over the group 1 flight route, especially near the surface where the averaged dust concentration from the TAS reaches near $200 \mu\text{g m}^{-3}$. Clearly, the model forecast has significantly underestimated the low level dust over the group 1 flight area.

3.3. Anthropogenic Dust Source

The problem of model underestimation of boundary layer dust had led us to re-examine the processes in the model that determine the dust distributions. We started by looking into the possible “missing source” over Asia. In our model, the dust emission is calculated using equation (1), where the source function S_d has been constructed according to the degree of topographical depression and the vegetation coverage [Ginoux et al. 2001]. The vegetation coverage was determined based on the 1987 AVHRR land cover data [DeFries and Townshend, 1994]. However, it has been recognized in recent years that China has become one of the countries with serious desertification disasters (e.g. United Nations Convention to Combat Desertification or UNCCD, <http://www.unccd.de>), especially in the Inner Mongolia Province. To test the possible impact of dust sources from the desertification regions, we have consulted maps on recent desertification areas from China [CCICCD, 1997], and estimated the dust sources over the Inner Mongolia Province in China, east of 110°E . These areas have been suffering from overgrazing and drought in recent years. As a consequence, they have become “bare soil” instead of “grassland” classified in the 1987 AVHRR land cover map. The modified dust emission in April 2001 is shown in Figure 9, with an additional dust size bin ($6 - 10 \mu\text{m}$) to reflect the fact that dust particles larger than $6 \mu\text{m}$ were commonly observed over Asia during dust storms (M.-X. Wang, IAP, Chinese Academy of Sciences, personal communication, 2001). The model calculated dust concentrations over the Yellow Sea with this modified dust source are shown in Figure 10 (dust concentrations for RF 6 and 13) and Figure 11 (group 1 flight averages of total dust), which are compared with the same observations shown in Figure 7b and 8a, respectively. Although including the $6 - 10 \mu\text{m}$ dust size bin has considerably increased the emission of total dust mass (comparing Figure 9 with Figure 1c), it is the addition of the Inner Mongolia desertification sources that has made a significant difference in model calculated dust vertical distributions over the Yellow Sea. This is because dust emitted from this region is readily advected to the Yellow Sea, contributing mostly to the low altitude dust loading. Compared to the model forecast products in Figure 7b and 8a, now the model agrees much better with the observations: The maximum dust concentrations in the boundary layer reach $300 \mu\text{g m}^{-3}$ for RF 6 and 13 (Figure 10), compared to about 80 and $10 \mu\text{g m}^{-3}$ respectively in the forecast (Figure 7b); for the group 1 flight averages, the R between the TAS dust and the model increases from -0.047 in the forecast (Figure 8a) to $+0.756$ now (Figure 11) and the S from 0.03 to 0.64.

4. Discussion

Chemistry transport models (CTM) have only recently become an integral part of field operations. For the ACE-Asia field experiment, three models participated in the intensive operational period to provide aerosol forecasts: the GOCART model, the Model of Atmospheric Transport and Chemistry (MATCH) of the National Center of Atmospheric Research, and the Chemical Forecast (CFORS) model of the University of Iowa and Kyushu University (see Huebert et al., 2003 for an overview). As the CTM will no doubt play increasingly important roles in future field experiments, it is important that we evaluate the model performance, the supporting process, and the strengths and limitations of the CTMs.

As shown in section 3, the most valuable contribution of a CTM forecast is that it offers direct information on quantities that are being measured, such as concentrations of individual aerosol species and precursor gases, extinctions and optical thickness of individual and total aerosols, vertical and horizontal distributions, and time variations of these species, to make the daily flight planning much more efficient than it would have been using the traditional weather forecast alone. Meanwhile, feedback from measurements provides enormous help to evaluate and improve the model. Our methods of model forecast skill verification presented in the previous section can be, in principle, applied to any model performance evaluation.

The most important quality of model products in supporting a field operation is the accuracy of predicted spatial and temporal distributions of the species. For the ACE-Asia field experiment, which was conducted over areas downwind of the sources where the loading and distributions of species are mainly controlled by transport, the model skill is critically dependant on the source locations where the pollutants and dust are originated and on the winds that move these species to the measurement locations. The degree of accuracy requirement, however, is different between the forecast phase during the field operation and data analysis phase after the mission, such that “quality” is more critical than “quantity” in the former, but both are equally important in the latter. The April 11 dust storm case illustrates that point. It was a forecast of the dust outbreak from the Gobi/Inner Mongolia region and heavy plumes transported to the Yellow Sea (Figure 4) that had guided the aircraft to the Yellow Sea on April 11 and 12 (RF 6 and RF 7). In this case, even though the forecast dust concentration was about 4 times lower than observations in the boundary layer (Figure 8b), the model forecast quality is still considered as “good” ($R = 0.76$, $S = 0.50$). However, good quality cannot be achieved if the vital sources are omitted, as illustrated in the case of April 24 (RF 13) in Figure 8b. Without the desertification sources over the central/eastern Inner Mongolia region, the model shows no skill of forecasting the heavy boundary layer dust over the Yellow Sea for RF 13. Only when the correct source locations are included is the model able to produce reasonable aerosol vertical profiles (Figure 10 and 11).

When verifying the model forecast skill in the previous section, we compared model results with 10-min merged data from the C-130 aircraft. Although our model resolution (about 200 km) is 3 – 4 times coarser than the spatial scale of the 10

min aircraft coverage (60 – 70 km at cruise altitude), it has demonstrated considerable skills in predicting the spatial and temporal variations of meteorological parameters and aerosol distributions. Yet, one should not expect the model to resolve fine structures detected by high frequency instruments. For example, in a few cases where some very well defined, stratified aerosol layers were observed [e.g. Redemann et al., 2003], the model was unable to resolve these fine layer structures because of its coarse vertical resolution (0.8 to 1 km in the middle troposphere).

Although the ACE-Asia intensive operation was conducted in a limited area over the Yellow Sea and the Sea of Japan within 20°N – 45°N and 124°E – 140°E domain, a global model displays a clear advantage in supporting such a limited area field experiment. First, our global model takes into account the transport of species from outside of the Asian regional domain to the measurement area (and thus produces more comprehensive forecast products). Our analysis has found that dust from Africa and pollution from Europe often made their ways into the Asia continent and western Pacific, contributing to the total aerosol loading over the Asia-Pacific region [Chin and Ginoux, 2002; P. Ginoux, manuscript in preparation]. Second, the model tracks the long-range transport of large aerosol plumes after they leave the source regions (thus the impact of regional sources on a larger scale). This is particularly relevant in springtime at mid-latitudes, when the prevailing westerly winds can effectively transport aerosols and pollutants from one continent to another. As shown in Figure 4, Asian dust during the large outbreak episodes does make a hemispheric scale impact. Third, a global model forecast is instrumental in coordinating field experiments simultaneously conducted in different geographic locations. For example, in April 2001, the Photochemical Ozone Budget of the eastern North Pacific Atmosphere-2 (PHOEBIA-2) field experiment on the west coast of the U.S. measured CO and aerosols that had significant fraction from long-range transport from Asia. The PHOEBIA-2 group also used our global forecast products (see Table 2) in their daily flight planning [D. Jaffe, University of Washington, personal communication, 2001], making their measurements in concert with ACE-Asia to address the issue of intercontinental transport.

5. Conclusions

We have used the GOCART model and the meteorological forecast fields from the GEOS DAS to provide aerosol forecast supporting the ACE-Asia field experiment in spring 2001. Our forecast offers direct information on aerosol optical thickness and concentrations, enabling effective flight planning, while feedbacks from measurements allow us to constantly evaluate the model, making successful model improvements. Close interaction between the modelers and measurement teams is essential in achieving mission objectives.

We have verified the model forecast skill by comparing the model prediction of dust, sulfate, and SO₂ concentrations, total aerosol extinction, and meteorological fields with those quantities actually measured by the C-130 aircraft during the ACE-Asia intensive operation period. The GEOS-3

meteorological forecast system has shown excellent skills in predicting winds, relative humidity, and temperature for the overall ACE-Asia experiment area as well as for each individual flight, with skill scores usually in the range of 0.7 – 0.99. The model is also skillful in forecasting pollution aerosols, with most scores above 0.5. The outbreak events of dust and their trans-Pacific transport have been well predicted by the model, but the model forecast constantly missed the boundary layer dust, especially over the Yellow Sea where heavy boundary layer dust were observed. We have attributed this mis-forecast of boundary layer dust to the fact that the model did not take into account the severe desertification regions in the central and eastern Inner Mongolia Province in China that has developed in recent decades due mainly to overgrazing and drought. After incorporating the desertification sources, the model is able to reproduce the observed high dust concentrations at lower altitudes. Thus, a successful model forecast operation depends critically on the correct source locations that determine where the emissions take place, and on realistic forecast winds and convection that decide where the aerosols are transported.

We have demonstrated that our model can adequately forecast the aerosol distributions and variations at the spatial and time scales of individual aircraft flight and, in the mean time, effectively account for the intercontinental transport of aerosols to place the ACE-Asia experiment into a larger regional to hemispheric context. Finally, the model should be an ideal tool in coordinating experiments that are taking place at different geographic locations and in integrating aircraft measurements with surface and satellite observations.

Acknowledgments. This work was supported by the NASA Radiation Science Program and ACPMAP (MC) and the NSF Atmospheric Chemistry Program (BH, TA, SM, AB, MC). We thank Thomas Owens and Doug Collins at the Goddard Data Assimilation Office and SAIC for providing the GEOS-3 forecast products during the ACE-Asia field operation. We thank reviewers for their constructive comments. This research is a contribution to the International Global Atmospheric Chemistry (IGAC) Core project of the International Geosphere Biosphere Program (IGBP) and is part of the IGAC Aerosol Characterization Experiments (ACE).

References

- Anderson, T. L., S. J. Masonis, D. S. Covert, N. C. Ahlquist, S. G. Howell, A. D. Clarke, and C. S. McNaughton, Variability of aerosol optical properties derived from in-situ aircraft measurements during ACE-Asia, *J. Geophys. Res.*, in press, 2003.
- Chinese Committee for Implementation of the Convention to Combat Desertification (CCICDD) Report, Beijing, 1997.
- Chin, M., R. B. Rood, S.-J. Lin, J.-F. Müller, and A. M. Thompson, Atmospheric sulfur cycle in the global model GOCART: Model description and global properties, *J. Geophys. Res.*, **105**, 24,661–24,687, 2000a.
- Chin, M., D. Savoie, B. J. Huebert, A. R. Bandy, D. C. Thornton, T. S. Bates, P. K. Quinn, E. S. Saltzman, and W. J. De Bruyn, Atmospheric sulfur cycle in the global model GOCART: Comparison with field observations and regional budgets, *J. Geophys. Res.*, **105**, 24,689–24,712, 2000b.
- Chin, M., P. Ginoux, S. Kinne, O. Torres, B. N. Holben, B. N. Duncan, R. V. Martin, J. A. Logan, A. Higurashi, and T. Nakajima, Tropospheric aerosol optical thickness from the GOCART model and comparisons with satellite and sunphotometer measurements, *J. Atmos. Sci.*, **59**, 461–483, 2002.
- Chin, M., and P. Ginoux, From regional emissions to global atmospheric change: Intercontinental transport of aerosols in the context of ACE-Asia, paper presented at the IGAC 2002 Conference, Crete, Greece, September 2002.
- Cooke, W. F., C. Liousse, H. Cachier, and J. Feichter, Construction of a 1x1 fossil fuel emissions data set for carbonaceous aerosol and implementation and radiative impact in the ECHAM4 model, *J. Geophys. Res.*, **104**, 22,137–22,162, 1999.
- d’Almeida, G. A., *Atmospheric Aerosols*, A. Deepak publishing, 561 pp, 1991.
- DeFries, R. S., and J. R. G. Townshend, NDVI-derived land cover classification at a global scale, *Int. J. Remote Sens.*, **15**, 3567–3586, 1994.
- Duncan, B. N., R. V. Martin, A. C. Staudt, R. Yevich, and J. A. Logan, Interannual and seasonal variability of biomass burning emissions constrained by remote-sensed observations, *J. Geophys. Res.*, **108**, 4040, doi:10.1029/2002JD002378, 2003.
- Ginoux, P., M. Chin, I. Tegen, J. Prospero, B. Holben, O. Dubovik, and S.-J. Lin, Sources and global distributions of dust aerosols simulated with the GOCART model, *J. Geophys. Res.*, **106**, 20,255–20,273, 2001.
- Gong, S., L. A. Barrie, and J.-P. Blanchet, Modeling sea salt aerosols in the atmosphere. 1: Model development, *J. Geophys. Res.*, **102**, 3805–3818, 1997.
- Herman, J. R., P. K. Bhartia, O. Torres, C. Hsu, C. Seftor, and E. Celarier, Global distribution of UV-absorbing aerosols from Nimbus 7/TOMS data, *J. Geophys. Res.*, **102**, 16,991–16,992, 1997.
- Hsu, N. C., J. R. Herman, P. K. Bhartia, C. J. Seftor, O. Torres, A. M. Thompson, J. F. Gleason, T. F. Eck, and B. N. Holben, Detection of biomass burning smoke from TOMS measurements, *Geophys. Res. Lett.*, **23**, 745–748, 1996.
- Huebert, B. J., T. Bates, P. B. Russell, G. Shi, Y. J. Kim, K. Kawamura, G. Carmichael and T. Nakajima, An overview of ACE-Asia: strategies for quantifying the relationships between Asian aerosols and their climatic impacts, submitted to *J. Geophys. Res.*, 2003.
- Köpke, P., M. Hess, I. Schult, and E. P. Shettle, Global aerosol data set, Tech. Rep. 243, Max-Planck Institute, 44 pp., 1997.
- Li-Jones, X., H. B. Maring, and J. M. Prospero, Effect of relative humidity on light scattering by mineral dust aerosol as measured in the marine boundary layer over the tropical Atlantic Ocean, *J. Geophys. Res.*, **103**, 31,113–31,121, 1998.
- Monahan, E. C., D. E. Spiel, and K. L. Davidson, A model of marine aerosol generation via whitecaps and wave disruption, in *Oceanic Whitecaps*, edited by E. C. Monahan and G. MacNiocaill, D. Reidel, pp. 167–174, 1986.
- Olivier, J. G. J., et al, Description of EDGAR version 2.0: A set of global emission inventories of greenhouse gases and ozone-depleting substances for all anthropogenic and most natural sources on a per country bases and on 1x1 grid, RIVM/TNO Rep. 771060-002, 140 pp., 1996.
- Redemann, J., S. Masonis, B. Schmid, T. Anderson, P. Russell, J. Livingston, O. Dubovik, and A. Clarke, Clear-column closure studies of aerosols and water vapor aboard the NCAR C-130 in ACE-Asia, 2001, *J. Geophys. Res.*, in press, 2003.
- Taylor, K. E., Summarizing multiple aspects of model performance in a single diagram, *J. Geophys. Res.*, **106**, 7183–7192, 2001.
- Torres, O., P. K. Bhartia, J. R. Herman, Z. Ahmad, and J. Gleason, Derivation of aerosol properties from satellite measurements of backscattered ultraviolet radiation: Theoretical bases, *J. Geophys. Res.*, **103**, 17,099–17,110, 1998.
- Weber, R. J., D. Orsini, Y. Daun, Y.-N. Lee, P. Klotz, and F. Brechtel, A particle-into-liquid collector for rapid measurements of aerosol chemical composition, *Aerosol Sci. Tech.*, **35**, 718–727, 2001.
- Zhang, X. Y., S. L. Gong, Z. X. Shen, F. M. Mei, X. X. Xi, L. C. Liu, Z. J. Zhou, D. Wang, Y. Q. Wang, Y. Cheng, Characterization of soil dust aerosol in China and its transport/distribution during 2001 ACE-Asia, *J. Geophys. Res.*, accepted, 2003.

T. Anderson and S. Masonis, Department of Atmospheric Sciences, University of Washington, Seattle, WA 98195 (tadand@atmos.washington.edu, sarahd@atmos.washington.edu).

A. Bandy and D. Thornton, Department of Chemistry, Drexel University, Philadelphia, PA 19104 (bandyar@drexel.edu, dct@drexel.edu).

B. Blomquist and B. Huebert, Dept. of Oceanography, University of Hawaii, Honolulu, HI 96822 (blomquis@hawaii.edu, huebert@hawaii.edu).

M. Chin, NASA Goddard Space Flight Center, Code 916, Greenbelt, MD 20771, USA (chin@rondo.gsfc.nasa.gov).

P. Ginoux, NOAA Geophysical Fluid Dynamics Laboratory, Princeton, NJ (pag@gfdl.noaa.gov).

R. Lucchesi, NASA Goddard Space Flight Center, Code 910.3, Greenbelt, MD 20771 (rlucchesi@dao.gsfc.nasa.gov).

R. Weber, School of Earth and Atmospheric Sciences, Georgia Institute of Technology, Atlanta, GA 30332 (rweber@eas.gatech.edu).

(Received March 27, 2003; accepted June 3, 2003).

¹ School of Earth and Atmospheric Sciences, Georgia Institute of Technology, Atlanta, Georgia, USA.

² Now at Atmospheric Chemistry and Dynamics Branch, NASA Goddard Space Flight Center, Greenbelt, Maryland, USA.

³ Now at NOAA Geophysical Fluid Dynamics Laboratory, Princeton, New Jersey, 08542, USA.

⁴ Science Applications International Corporation, Beltsville, Maryland, USA.

⁵ Also at Data Assimilation Office, NASA Goddard Space Flight Center, Greenbelt, Maryland, USA.

⁶ Department of Oceanography, University of Hawaii, Honolulu, Hawaii, USA.

⁷ Department of Atmospheric Sciences, University of Washington, Seattle, Washington, USA.

⁸ Department of Chemistry, Drexel University, Philadelphia, Pennsylvania, USA.

Figure 1. Emissions of aerosols and precursor gases in April 2001 used in the GOCART forecast mode: (a) sulfur (DMS + SO₂), (b) carbonaceous (BC + OC), (c) dust, and (d) sea-salt.

Figure 2. Schematic of the GOCART model forecast process during ACE-Asia.

Figure 3. The GOCART model aerosol forecast of sulfate (left column) and dust (right column) AOT at 500 nm on April 2 (top row) and April 12 (bottom row), 2001.

Figure 4. The GOCART model forecast of dust evolution and trans-Pacific transport (shown as AOT, left column) and TOMS AI (right column) on April 8 (top row), April 11 (middle row), and April 14 (bottom row), 2001.

Figure 5. The C-130 flight track during ACE-Asia intensive field operation period.

Figure 6. The model forecast skill score (S , closed circles) and the correlation coefficients (R , open circles) between the forecast and observed quantities for the 19 research flights conducted with the C-130 aircraft: Wind speed, wind direction (clockwise with 0° as winds from the north), relative humidity, temperature, concentrations of sub-micron dust (PILS) and sulfate (PILS), SO₂, and total aerosol extinction at 550 nm. The number of total data points in each flight is indicated at the bottom of each panel. Only R values are shown for dust because the model predicted total dust and most dust particles are in super-micron size range while the PILS measured only sub-micron particles. See text for details.

Figure 7a. Vertical profiles of forecast (crosses) and observed (circles and triangles) concentrations of dust (1st row), sulfate (2nd row), SO₂ (3rd row), and aerosol extinction (4th row) for the C-130 RF 4, 9, 14, and 16 when the dust influence was minimum. For sulfate and dust, data from the TAS are shown in gray circles and from the PILS in triangles. The R , E , and S (with *) are related to the PILS data only. See text for details.

Figure 7b. Same as Figure 7a, but for the C-130 RF 5, 6, 10, and 13 when heavy dust was encountered.

Figure 8a. Averaged vertical profiles of forecast (crosses) and observed (circles) meteorological variables and concentrations of dust, sulfate, SO₂, and aerosol extinction from the group 1 C-130 flights (RF 4, 6, 7, 10, 13, 14, 15, and 18) over the Yellow Sea. The correlation coefficient (R), root-mean-square error (E), and the model forecast skill score (S) are indicated in each plot except for the PILS sub-micron dust where only R is shown.

Figure 8b. Same as Figure 8a, but for the group 2 C-130 flights (the remaining 11 flights not included in Figure 8a).

Figure 9. Dust emission in April 2001 after adding the desertification sources in the Inner Mongolia Province and extended dust particle size to 10 μm (compared to Figure 1c).

Figure 10. Vertical profiles of modeled and observed dust concentrations for RF 6 and 13. The model results are calculated with the modified dust sources (Figure 9). Symbols are the same as in Figure 7. This figure should be compared with Figure 7b where the model forecasts are shown.

Figure 11. Averaged vertical profiles of modeled and observed dust concentrations from the group 1 C-130 flights (RF 4, 6, 7, 10, 13, 14, 15, and 18) over the Yellow Sea. The model results are calculated with the modified dust sources shown in Figure 9. The observations are from the TAS instruments (i.e. total dust). Symbols are the same as in Figure 8. This figure should be compared with Figure 8a for the TAS dust (1st panel in the 2nd row) where the model forecast is shown.

Table 1. GEOS-3 products used in the GOCART model.

Name	Description	Dim	Time	Qty*
PS	Surface pressure (hPa)	2-D	3-hr	Inst
SLP	Sea level pressure (hPa)	2-D	3-hr	Inst
SURFTYPE	Surface types (water, land, ice, etc.)	2-D	3-hr	Inst
GWET	Soil moisture (% of field capacity)	2-D	3-hr	Inst
TROPP	Tropopause pressure (hPa)	2-D	3-hr	Inst
UWND	Zonal wind (m s^{-1})	3-D	6-hr	Inst
VWND	Meridional wind (m s^{-1})	3-D	6-hr	Inst
TMPU	Temperature (K)	3-D	6-hr	Inst
SPHU	Specific humidity (g kg^{-1})	3-D	6-hr	Inst
PREACC	Total precipitation (mm day^{-1})	2-D	3-hr	Avg
PRECON	Convective precipitation (mm day^{-1})	2-D	3-hr	Avg
HFLUX	Sensible heat flux (W m^{-2})	2-D	3-hr	Avg
TGROUND	Ground temperature (SST over water) (K)	2-D	3-hr	Avg
RADSWG	Net downward shortwave flux at ground (W m^{-2})	2-D	3-hr	Avg
ALBEDO	Surface albedo (0-1)	2-D	3-hr	Avg
USTAR	Friction velocity (m s^{-1})	2-D	3-hr	Avg
Z0	Surface roughness (m)	2-D	3-hr	Avg
PBL	Planetary boundary layer depth (hPa)	2-D	3-hr	Avg
U10M	Zonal wind at 10 meters (m s^{-1})	2-D	3-hr	Avg
V10M	Meridional wind at 10 meters (m s^{-1})	2-D	3-hr	Avg
TAUCLD	Cloud optical depth	3-D	6-hr	Avg
CLDTOT	Cloud fraction	3-D	6-hr	Avg
CLDRAS	Convective cloud fraction	3-D	6-hr	Avg
MOISTQ	Specific humidity tendency, moist ($\text{g kg}^{-1} \text{ day}^{-1}$)	3-D	6-hr	Avg
DQLS	Specific humidity tendency, stratiform ($\text{g kg}^{-1} \text{ day}^{-1}$)	3-D	6-hr	Avg
KH	Eddy diffusivity coefficient, scalars ($\text{m}^2 \text{ s}^{-1}$)	3-D	6-hr	Avg
CLDMAS	Cloud mass flux ($\text{kg m}^{-2} \text{ s}^{-1}$)	3-D	6-hr	Avg
DTRAIN	Detrainment cloud mass flux ($\text{kg m}^{-2} \text{ s}^{-1}$)	3-D	6-hr	Avg

*Quantity: Inst = instantaneous, Avg = average.

Table 2. GOCART model forecast products.

Forecast product	Forecast frequency
Latitude-longitude distributions:	
Optical thickness of individual and total aerosols	3 hour
Column burden (g m^{-2}) of individual aerosol species	3 hour
Latitudinal cross section at 125°E, 135°E, and 140°E:	
Total Aerosol extinction (km^{-1})	3 hour
Individual aerosol concentration (g m^{-3})	3 hour
Longitudinal cross section at 30°N and 40°N:	
Total Aerosol extinction (km^{-1})	3 hour
Individual aerosol concentration (g m^{-3})	3 hour
Meteorological variables (GEOS DAS):	
Low level (700 – 1000 mb), mid-level (400 – 700 mb), and high level (above 400 mb) cloud cover	3 hour
Total precipitation (mm day^{-1})	
Wind speed and direction at 0.1 km and 4 km	3 hour 6 hour
Global distributions:	
Optical thickness for individual and total aerosols	3 hour
Concentration of sulfate and dust at 0.1, 4, and 6 km	3 hour

Table 3. Datasets used for model forecast verification.

Quantity	Instrument	Data frequency	Investigator	Institute
Aerosol extinction at 550 nm, total	Nephelometer and absorption photometer	10 sec	T. Anderson S. Masonis	U. Washington
SO_4^{2-} , Ca^{2+} , $d < 1.3 \mu\text{m}$	Particle-Into-Liquid Sampler (PILS)	3 – 4 min	R. Weber D. Orsini K. Maxwell	Georgia Tech
SO_4^{2-} , Ca^{2+} , total	Total Aerosol Sampler (TAS)	20 – 60 min	B. Huebert J. Heath S. Howell T. Bertram J. Zhuang	U. Hawaii
SO_2	Atmospheric Pressure Ionization Mass Spectrometer (APIMS)	1 sec	A. Bandy D. Thornton B. Blomquist	Drexel U. U. Hawaii

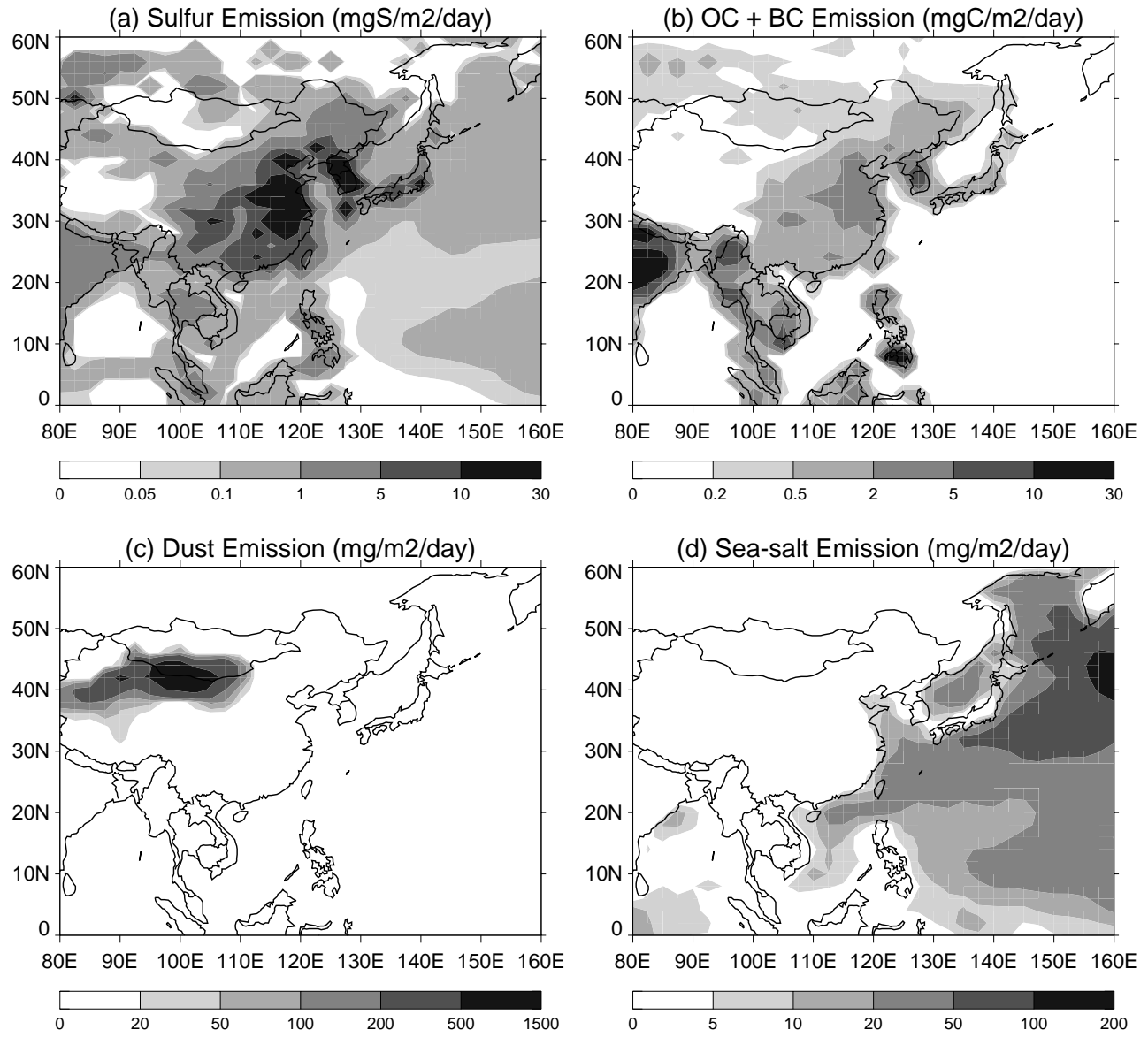


Figure 1

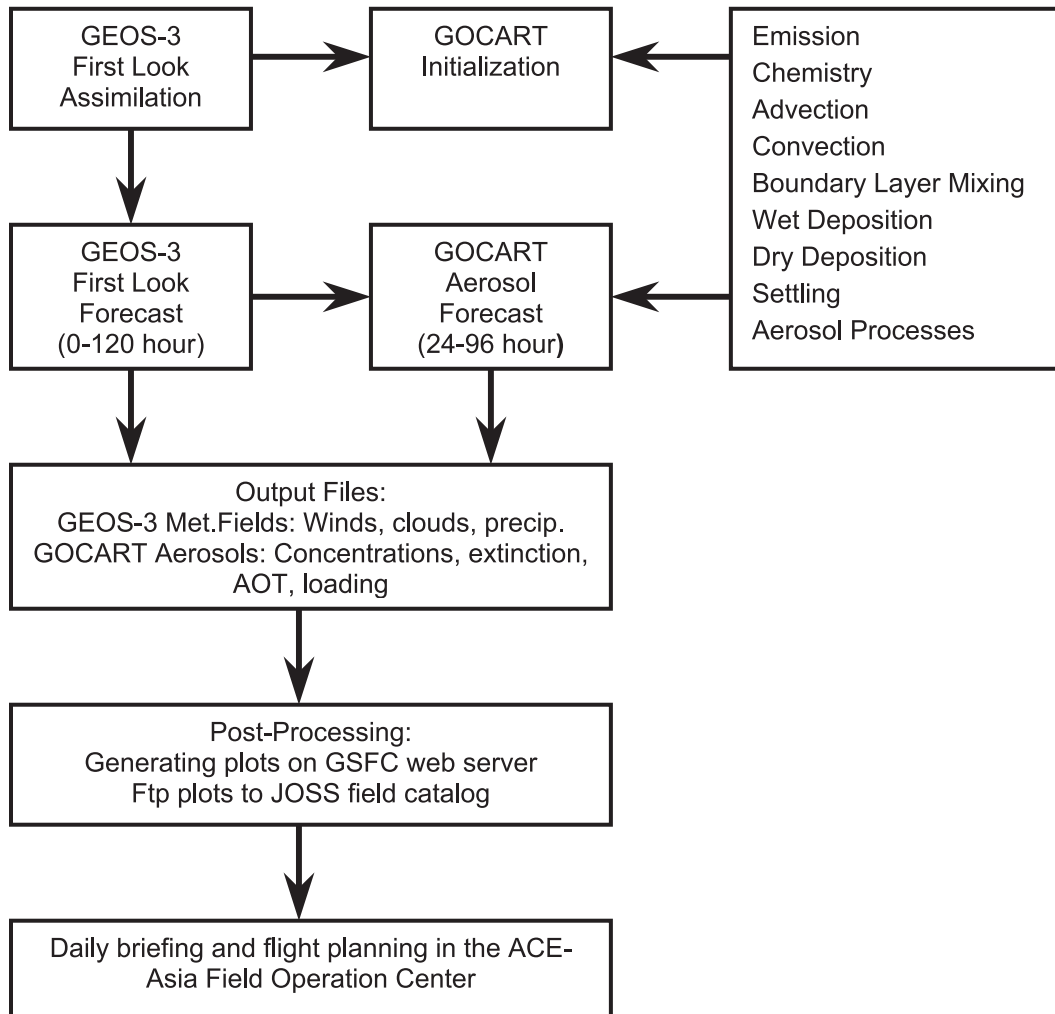


Figure 2

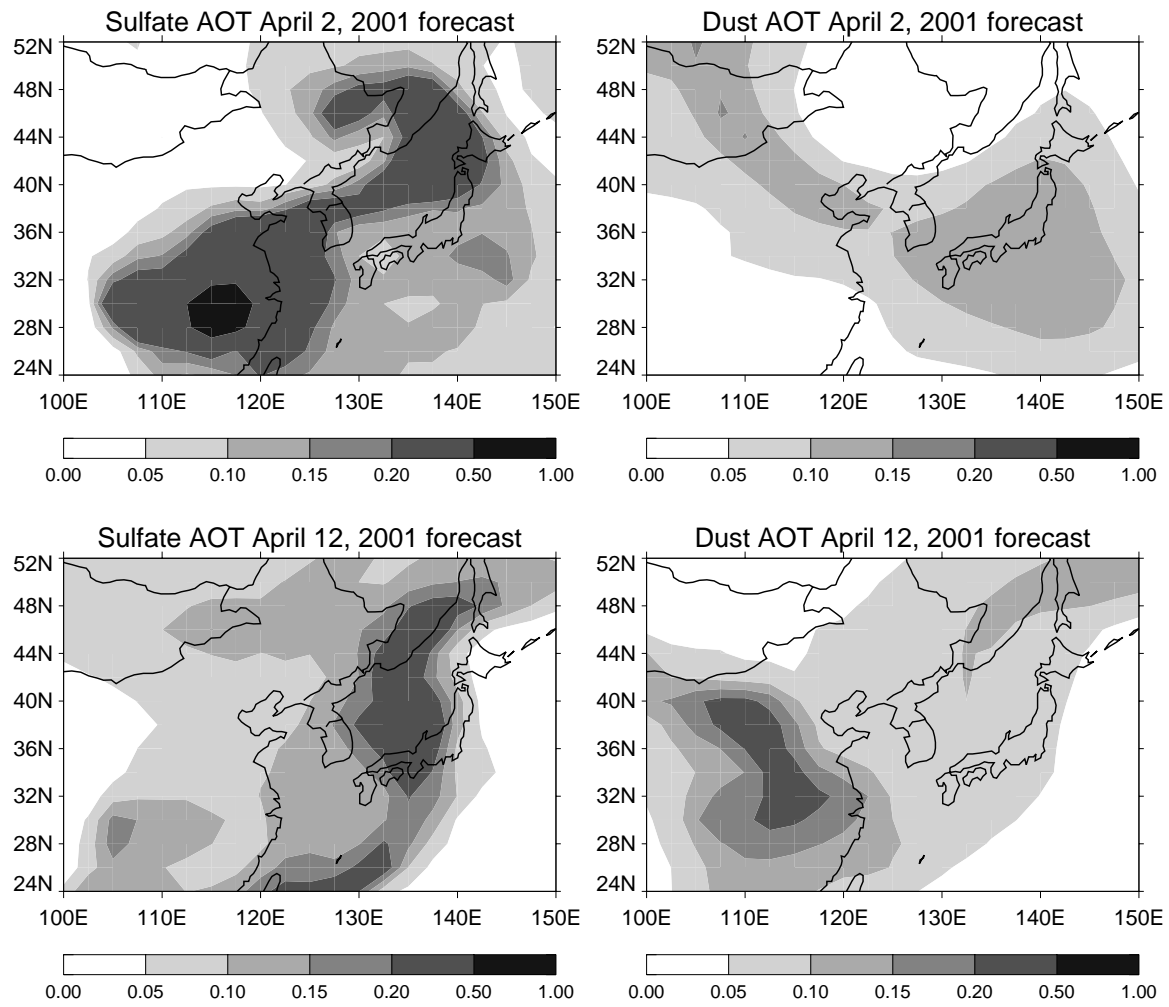


Figure 3

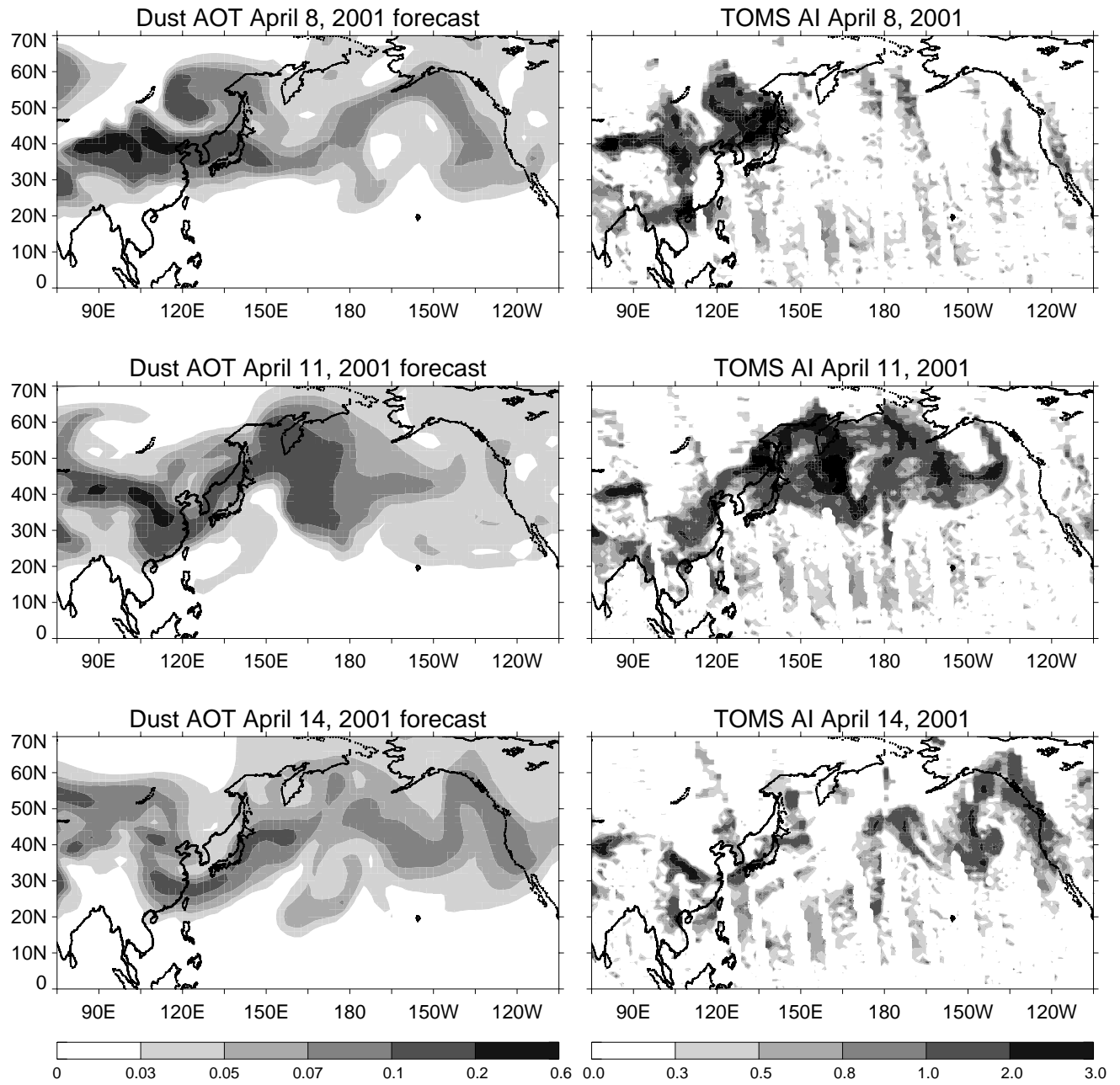


Figure 4

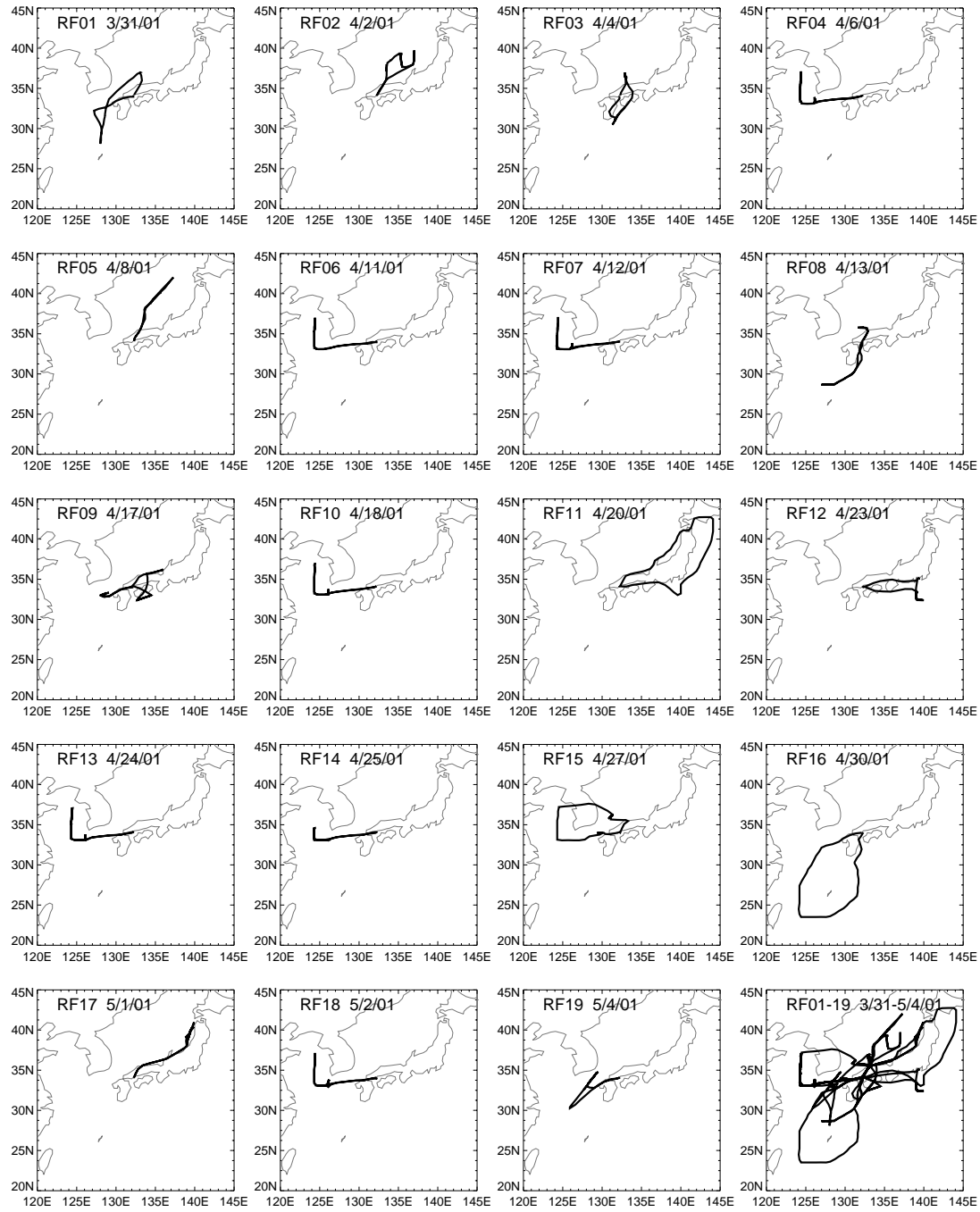


Figure 5

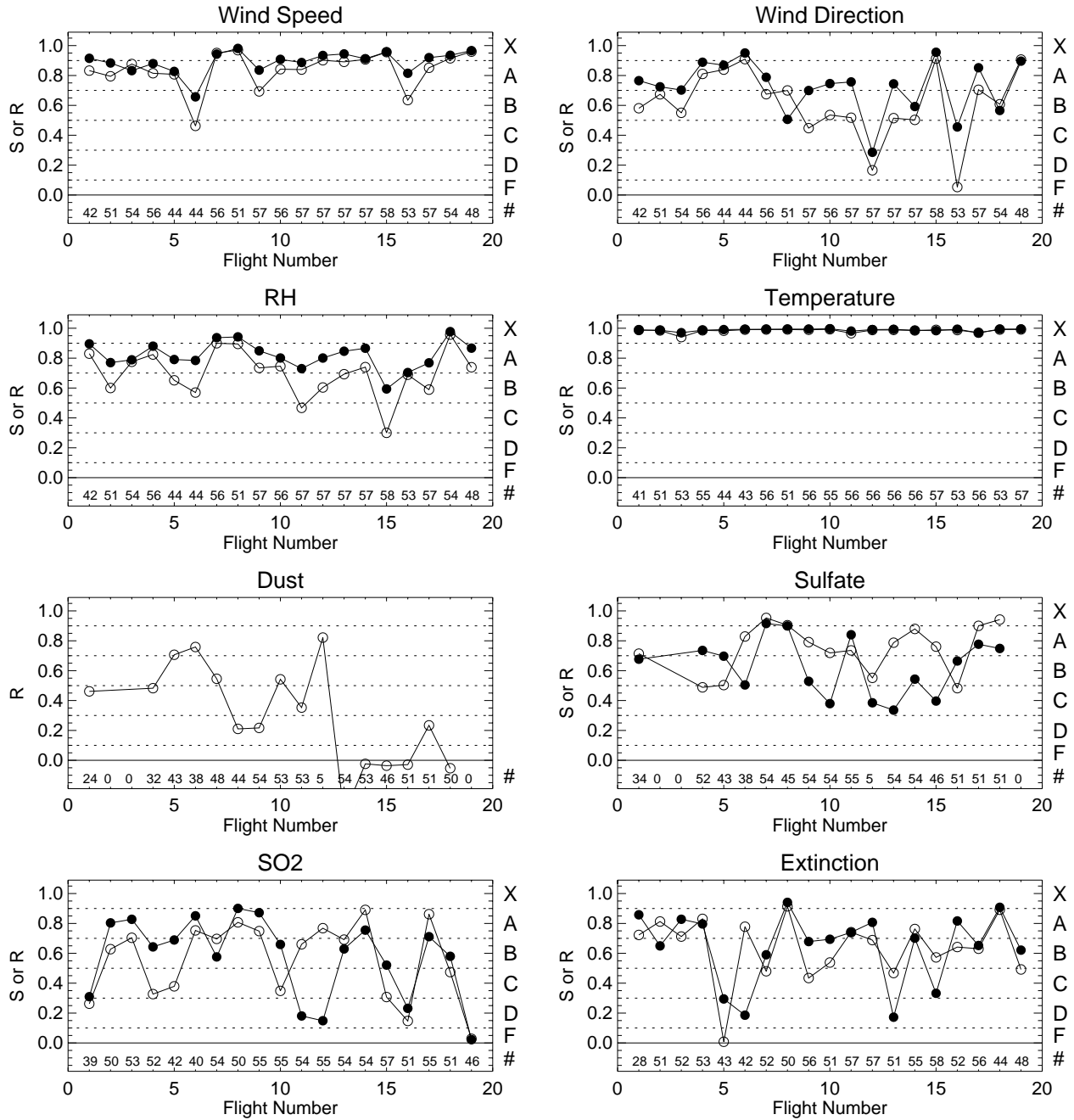


Figure 6

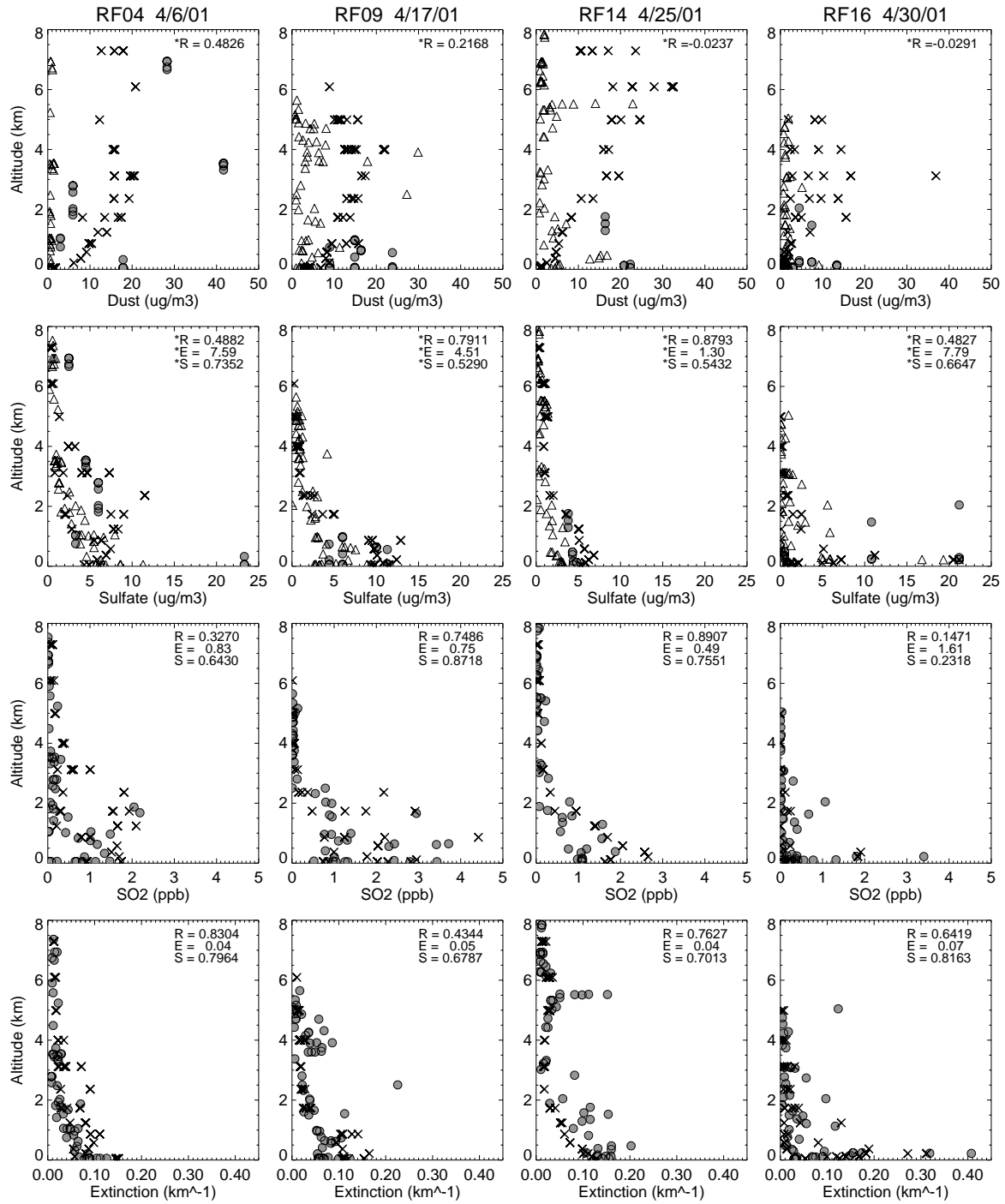


Figure 7a

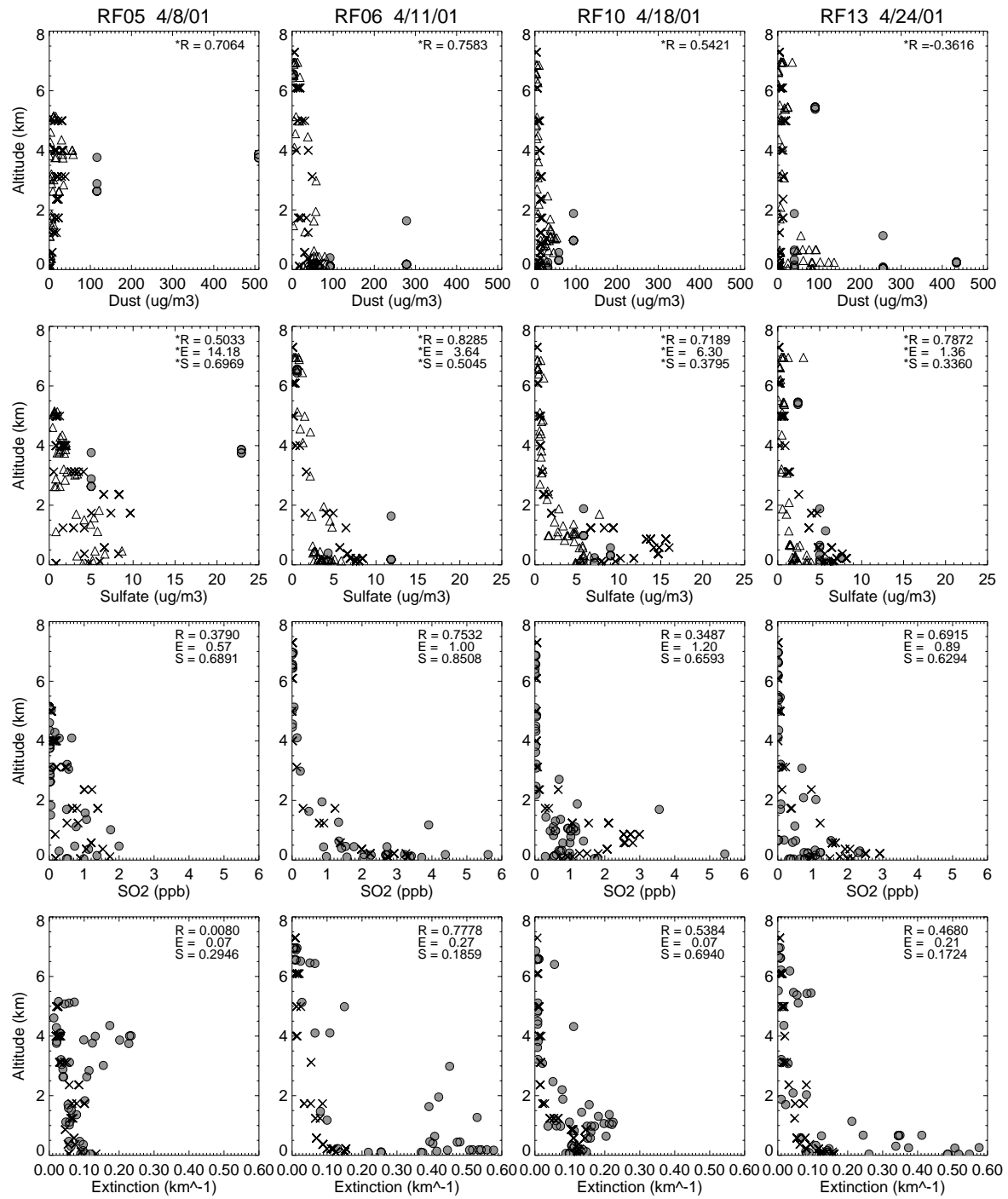


Figure 7b

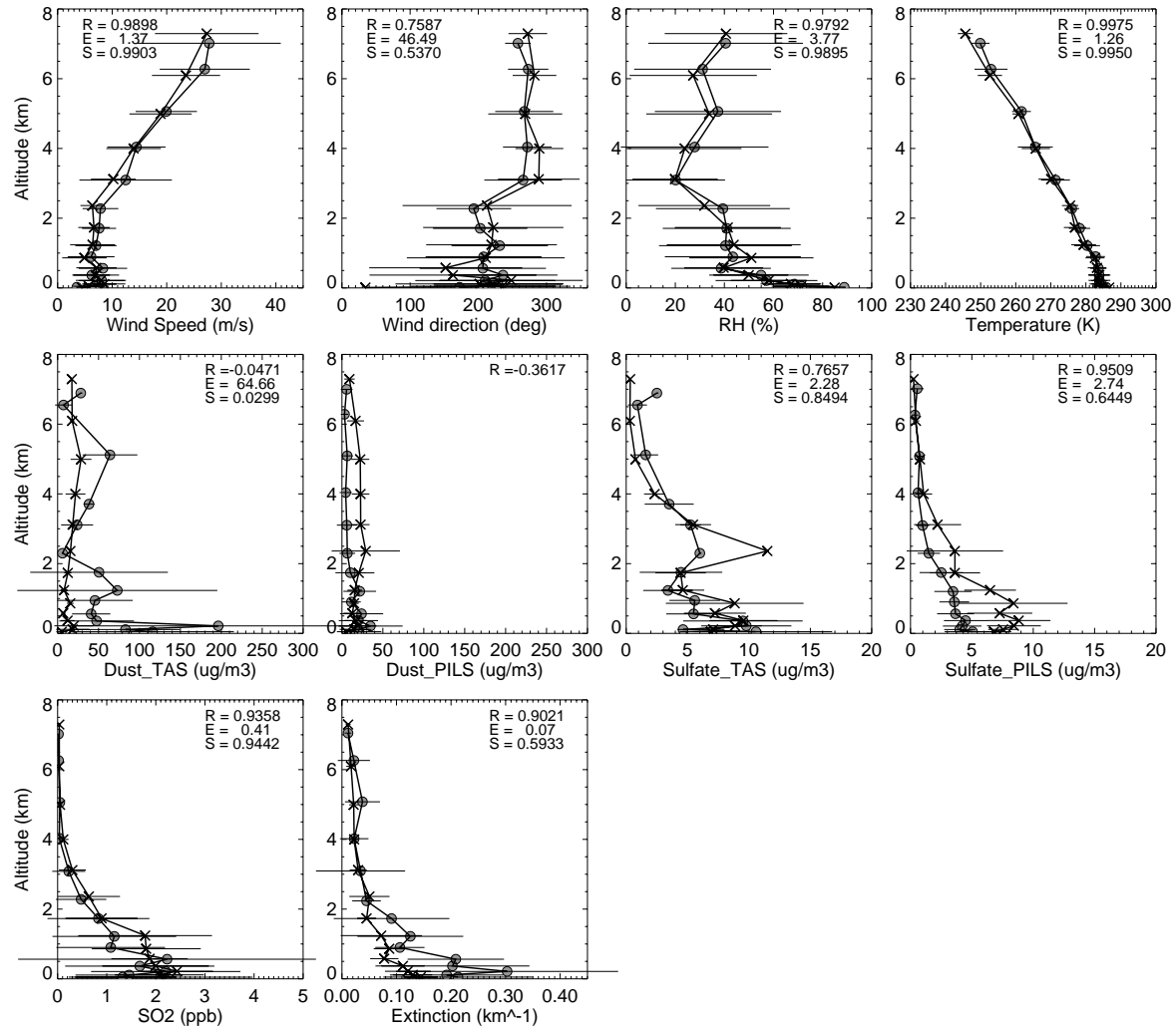


Figure 8a

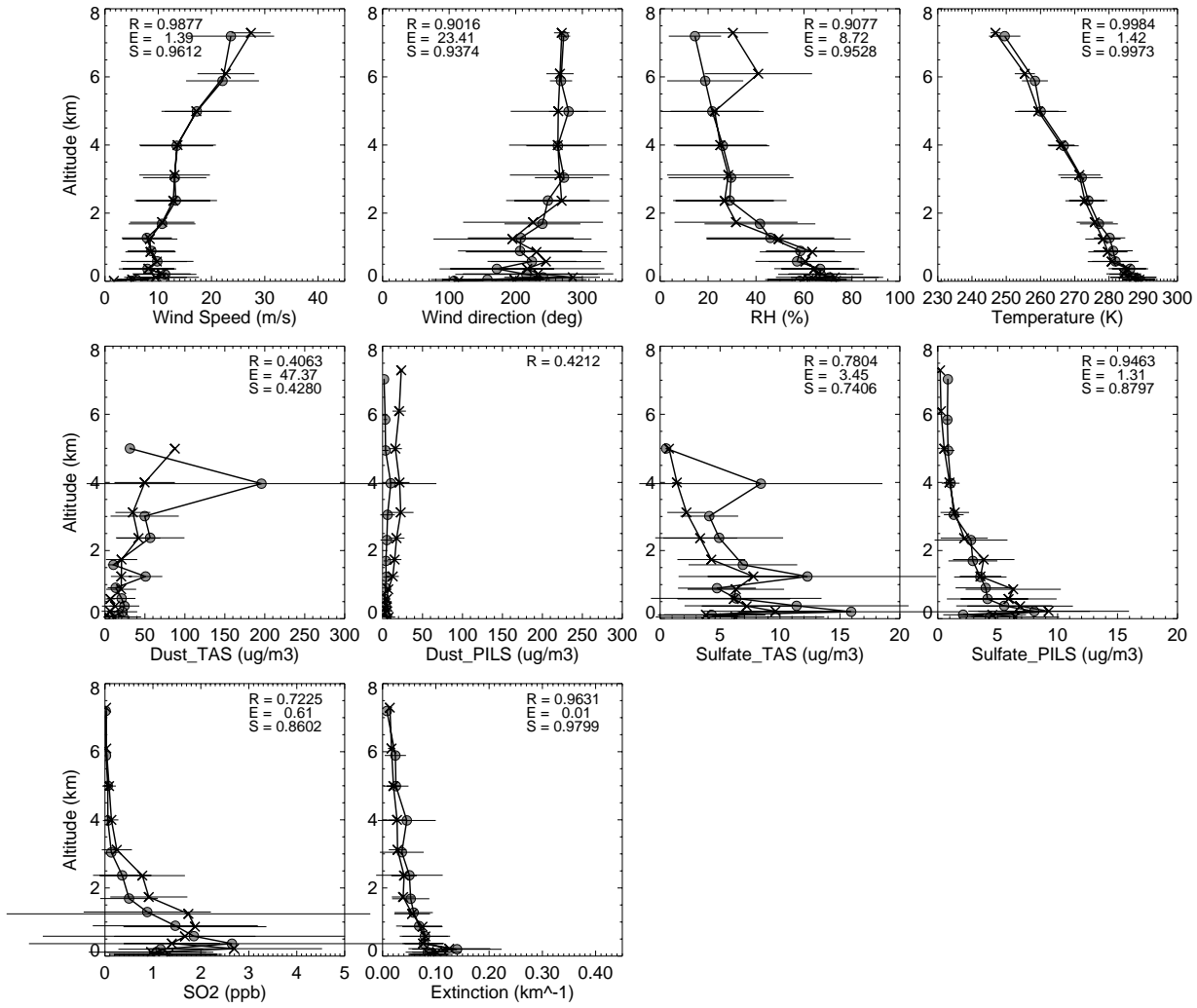


Figure 8b

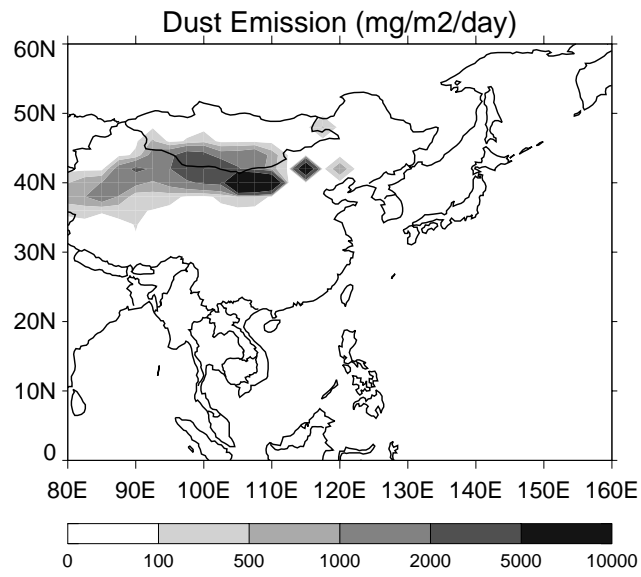


Figure 9

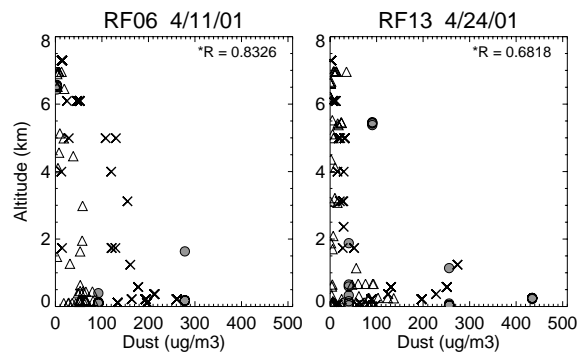


Figure 10

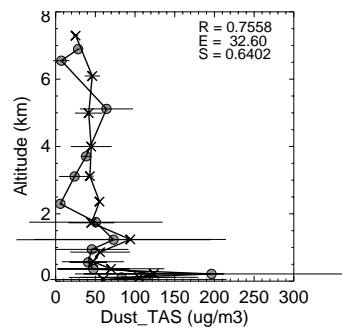


Figure 11